Mechanisms of Two-Electron and Four-Electron Electrochemical Oxygen Reduction Reactions at Nitrogen-Doped Reduced Graphene Oxide

Hyo Won Kim,[†,‡,§,⋈] Vanessa J. Bukas,[∥,⊥,¶,⋈] Hun Park,[#] Sojung Park,[▽] Kyle M. Diederichsen,[†,‡] Jinkyu Lim,[○] Young Hoon Cho,[◆] Juyoung Kim,[§] Wooyul Kim,[▽] Tae Hee Han,[#] Johannes Voss,[∥,⊥] Alan C. Luntz,[*,∥,⊥] and Bryan D. McCloskey[*,†,‡]

[†]Department of Chemical and Biomolecular Engineering, University of California, Berkeley, California 94720, United States

[‡]Energy Storage and Distributed Resources Division, Lawrence Berkeley National Laboratory, Berkeley, California 94720, United States

[§]Department of Advanced Materials Engineering, Kangwon National University, Samcheok 24341, Korea

[∥]SUNCAT Center for Interface Science and Catalysis, Department of Chemical Engineering, Stanford University, Stanford, California 94305-5025, United States

[⊥]SUNCAT Center for Interface Science and Catalysis, SLAC National Accelerator Laboratory, 2575 Sand Hill Road, Menlo Park, California 94025, United States

[#]Department of Organic and Nano Engineering, Hanyang University, Seoul 04763, Korea

[▽]Department of Chemical and Biological Engineering, Sookmyung Women's University, Seoul 04310, Korea

[○]Department of Chemical and Biomolecular Engineering, Korea Advanced Institute of Science and Technology, Daejeon 34141, Korea

[◆]Membrane Research Center, Korea Research Institute of Chemical Technology, Daejeon 34114, Korea

ABSTRACT: Doped carbon-based systems have been extensively studied over the past decade as active electrocatalysts for both the two-electron ($2e^-$) and four-electron ($4e^-$) oxygen reduction reactions (ORRs). However, the mechanisms for ORR are generally poorly understood. Here, we report an extensive experimental and first-principles theoretical study of the ORR at nitrogen-doped reduced graphene oxide (NrGO). We synthesize three distinct NrGO catalysts and investigate their chemical and structural properties in detail via X-ray photoelectron spectroscopy, infrared and Raman spectroscopies, high-resolution transmission electron microscopy, and thin-film electrical conductivity. ORR experiments include the pH dependences of $2e^-$ versus $4e^-$ ORR selectivity, ORR onset potentials, Tafel slopes, and H/D kinetic isotope effects. These experiments show very different ORR behavior for the three catalysts, in terms of both selectivity and the underlying mechanism, which proceeds either via coupled proton−electron transfers (CPETs) or non-CPETs. Reasonable structural models developed from density functional theory rationalize this behavior. The key determinant between CPET vs non-CPET mechanisms is the electron density at the Fermi level under operating ORR conditions. Regardless of the reaction mechanism or electrolyte pH, however, we identify the ORR active sites as sp^2 carbons that are located next to oxide regions. This assignment highlights the importance of oxygen functional groups, while details of (modest) N-doping may still affect the overall catalytic activity, and likely also the selectivity, by modifying the general chemical environment around the active site.

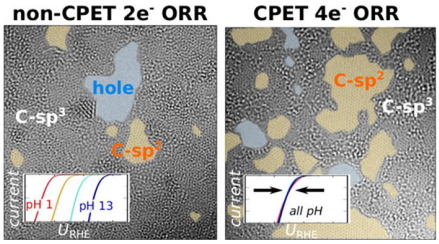

KEYWORDS: *electrocatalysis, oxygen reduction reaction, mechanism, selectivity, pH, kinetic isotope, nitrogen-doped reduced graphene oxide*

Oxygen electroreduction plays an important role in emerging energy and chemical applications, including acidic and alkaline fuel cells and the formation of hydrogen peroxide, a commodity oxidizing agent. In aqueous environments, the oxygen reduction reaction (ORR) can proceed through two overall reactions, which, in acidic solutions, are given as

$$O_2 + 4(H^+ + e^-) \Rightarrow 2H_2O \; U^0 = 1.23 \; V_{RHE} \quad (1)$$

$$O_2 + 2(H^+ + e^-) \Rightarrow H_2O_2\ U^0 = 0.70\ V_{RHE} \quad (2)$$

where U^0 is the standard equilibrium potential for the reactions[1] and V_{RHE} stands for the potential relative to the reversible hydrogen electrode (RHE). V_{RHE} is related to that of the standard hydrogen electrode (SHE) via $V_{RHE} = V_{SHE} + 0.0592$ pH at 300 K so that the thermodynamics of the reactions are independent of pH on the V_{RHE} scale. In basic solutions, H_2O becomes the proton donor and these equations become[1]

$$O_2 + 2H_2O + 4e^- \Rightarrow 4OH^-\ U^0 = 1.23\ V_{RHE} \quad (3)$$

$$O_2 + 2H_2O + 2e^- \Rightarrow H_2O_2 + 2OH^-\ U^0 = 0.70\ V_{RHE} \quad (4)$$

At pH > 11.7, eq 4 becomes[1]

$$O_2 + H_2O + 2e^- \Rightarrow HO_2^- + OH^-\ U_0 = 0.76\ V_{RHE} \quad (5)$$

Both $2e^-$ and $4e^-$ ORRs are important electrochemical processes: the $4e^-$ ORR (eqs 1 or 3) is the reaction that generally limits fuel cell efficiency, while the $2e^-$ electron ORR (eqs 2, 4, or 5) provides an electrochemical path for the production of hydrogen peroxide, an important industrial chemical.

In addition to traditional precious-metal (and precious-metal alloy) ORR electrocatalysts, carbon-based systems have also been extensively explored in the last decade since they hold promise as very cheap, abundant, and durable ORR electrocatalysts.[2] These include pure carbon in different forms (amorphous, glassy, graphite, graphene, fullerenes, nanotubes, nanoribbons) and carbon with different heteroatom substitutions.[2−7] These electrocatalysts yield a wide variety of electrochemical results, in terms of both ORR activity and selectivity.[2−7] In contrast to the simple metal electrocatalysts, understanding the origin of catalytic activity in these systems is quite challenging. Some of the challenges arise from the complex inhomogeneous structure of the carbon-based catalysts so that the identity of the electrocatalytically active site is not known. In addition, the detailed catalyst structure, which defines the activity and even selectivity, seems strongly dependent upon synthesis conditions. Last but not least, both activity and selectivity are sometimes found to change with electrolyte pH.[8,9] For example, ORR electrocatalysis at nitrogen-doped graphene has been intensively investigated, sometimes yielding $2e^-$ ORR and sometimes $4e^-$ ORR.[7,9] For these systems, in particular, there is much debate as to the identity of the catalytically active sites. Some argue that ORR activity originates due to graphitic N sites, while others argue that pyridinic or pyrrolic N sites are key.[3,6,7]

Understanding the mechanisms responsible for ORR in these nonmetal catalysts is the minimum required to aid in guiding the optimization of the electrocatalysts. ORR electrocatalytic activity has traditionally been described in terms of the thermodynamics of the surface-adsorbed intermediates (e.g., OH*, where * refers to surface-adsorbed species), with the potential dependence of the free energies of the reduction steps given by the computational hydrogen electrode $H^+ + e^- = 1/2\ H_2$.[10] This defines a limiting potential for the ORR, and plots of this limiting potential versus a descriptor such as OH* binding energy have been very successful in describing and predicting ORR activity volcanoes for metals and alloys, for both $2e^-$ and $4e^-$ ORRs.[11] This implicitly assumes that the mechanism for the ORR is based on a series of coherently coupled proton−electron transfers (CPETs), where an e^- and a H^+ are always transferred simultaneously with a single transition state. First-principles thermodynamics based on density functional theory (DFT) has been very successful in predicting activity trends for both $2e^-$ and $4e^-$ ORRs occurring at metal and alloy electrocatalysts.[11] However, the catalyst selectivity between $2e^-$ and $4e^-$ ORRs is not described by thermodynamics since this always favors the $4e^-$ ORR.[12] It has been suggested that the relative height of kinetic barriers for the CPET reduction of OOH* to form either H_2O_2 or O* + H_2O (or 2OH*) defines the selectivity within this conceptual framework.[11] However, the calculation of CPET barriers that are accurate enough to explain selectivity appears to be currently beyond the state of the art.[13]

We have recently presented a combination of comprehensive first-principles theory and experiment that unravels the mechanism behind the $2e^-$ ORR to produce H_2O_2 on a catalyst composed of mildly reduced graphene oxide supported on P50 carbon paper (mrGO/P50).[14] This catalyst is unique, in that it shows > 99% selectivity toward H_2O_2 in both alkaline and acidic electrolytes. Activity, however, is a strong function of pH. A high gravimetric activity and essentially zero overpotential at pH = 13 were observed.[15] While mrGO/P50 is thus an excellent H_2O_2 catalyst in base, it shows a significant (∼1 V) overpotential in acidic electrolytes. This dramatic difference was fully explained by revealing the underlying ORR mechanism. Because mrGO is semiconducting, the ORR mechanism cannot be based on the conventional CPET mechanism as typical for metals. Instead, we presented experimental and theoretical evidence that identifies the potential-limiting step as an outer-sphere electron transfer to O_2 in solution to produce O_2^-(aq). This is initiated from a conducting support (such as the P50 carbon paper) and gives rise to the considerable activation (onset) overpotential measured in acid. This step is followed by the adsorption of either O_2^-(aq) or HO_2(aq) (formed by the protonation of O_2^-(aq)) at the mrGO active site, depending upon the pH of the electrolyte. Subsequent decoupled proton and electron transfers then ultimately produce H_2O_2 (eqs 2 and 4) or HO_2^- (eq 5) depending upon pH. We henceforth refer to this type of mechanism as non-CPET to indicate that an e^- and a H^+ are transferred in a nonconcerted, stepwise fashion so that two transition states are involved (regardless of the order in which these transfers occur). Because both the conductive substrate, which in the experiments was P50 carbon paper, and the mrGO are necessary for the catalytic activity, we have called the mrGO/P50 a cocatalyst.

To extend the knowledge on both $2e^-$ and $4e^-$ ORR mechanisms of carbon-based materials, here we synthesize three different nitrogen-doped reduced graphene oxide (NrGO) catalysts and investigate their chemical and structural properties in detail. We then combine experiment and theory to investigate their ORR properties when supported on conducting carbon paper (P50). The goal is to unravel the underlying catalytic mechanisms and ultimately to understand how this influences ORR activity and selectivity. We emphasize that these materials have two heteroatom substitutions in graphene, both oxygen and nitrogen, so that it is not immediately apparent which heteroatom leads to the ORR active site.

RESULTS

NrGO Electrocatalyst Characterization. NrGO-2, NrGO-3, and NrGO-4 are synthesized as discussed in the Experimental Section of the Supporting Information. Detailed characterization via C 1s, N 1s, and O 1s of X-ray photoelectron spectroscopy (XPS) of the three catalysts is presented in Figure S1, with the atomic compositions and dominant bonding components summarized in Table 1. While

Table 1. Elemental Composition of NrGO Electrocatalysts Based on C 1s, O 1s, and N 1s XPS and Summary of Critical Carbon-, Oxygen-, and Nitrogen-Bonding Fractions Based on XPS Line Shape Decomposition

	NrGO-2	NrGO-3	NrGO-4
C/N/O (atomic %)	76:11:13	87: 3: 10	88: 3: 9
sp^2 carbon/total C	0.54	0.63	0.73
O−C aromatic/total O	0.39	0.38	0.67
graphitic N/total N	0.25	0.50	0.51

the atomic concentrations are accurately determined via the XPS, the decomposition of atomic species into bonding components is only approximate because of their strong overlap in the XPS spectra. In addition, the decomposition of the bonding components is based on a comparison to rGO XPS spectra (for carbon and oxygen) and to nitrogenated graphene (for nitrogen), rather than reference studies on actual NrGO species. There are certainly differences in both the elemental composition of the three catalysts and its detailed bonding components. However, the dominant difference seems to be that the sp^2 carbon fraction increases along the series (in order) NrGO-2 to NrGO-3 to NrGO-4. This observation is in line with an increasing fraction of oxygen that is assigned as bonded to the aromatic carbon, i.e., the type of O−C bonds that are expected to dominate the boundaries of graphene domains by graphene oxide domains.

This finding is consistent with comparing the average size of sp^2 ring clusters (L_a) that are obtained from the carbon Raman spectra for the three samples (Figure S2). L_a is known to scale with $\sqrt{I_D/I_G}$, where I_D and I_G are the integrated intensities of the D and G carbon Raman bands, respectively (derived from integrating the corresponding peak areas).[16] Here, we estimate this factor as $\sqrt{I_D/I_G}$ ~1.29 for NrGO-2, ~1.32 for NrGO-3, and ~1.37 for NrGO-4. This suggests an increasing fraction of sp^2 carbon along this series, in agreement with the trend extracted from the XPS decompositions.

Similar conclusions can also be inferred from the high-resolution transmission electron microscopy (HR-TEM) (Figures 1a and S3). The TEM images clearly indicate the existence of discrete sp^2 carbon and sp^3 carbon (e.g. graphene oxide) domains in all catalyst surfaces that are separated from one another, but with varying amount and size of the sp^2 domains. While the TEM images represent only a small region of the overall surface, we believe that these images are representative of the entire catalyst surfaces. Therefore, NrGO-2 and NrGO-4 are characterized as "poorest" and "richest" in sp^2 carbon morphologies, respectively, while NrGO-3 represents an intermediate state between these two extrema. Edges outlining these domains are largely decorated principally by oxygen heteroatoms, as evidenced by the white spots appearing along the sp^2 carbon patch boundaries.[17] This observation is consistent with the XPS analysis regarding the

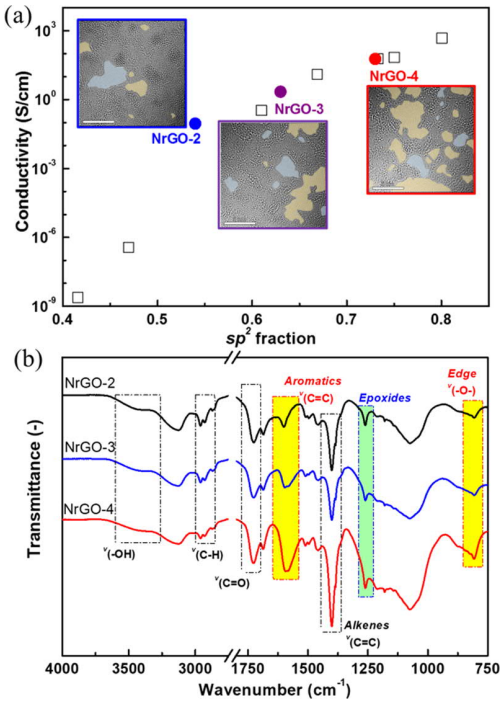

Figure 1. Physical and chemical results of NrGO catalysts. (a) Solid circles represent the electrical conductivity of 50 nm films of NrGO catalysts vs the sp^2 fraction of the total number of carbon atoms as determined by XPS. White squares are the electrical conductivity of three-monolayer films of rGO vs the carbon sp^2 fraction, from the work of Chhowalla and co-workers (data reproduced with permission from John Wiley and Sons).[20] The insets show the representative HR-TEM of the three catalysts (larger versions of these images can be found in Figure S3). The orange regions cover the largest nm-sized sp^2 carbon patches and the blue regions indicate holes in the platelet. The gray regions are mostly sp^3 carbon. (b) IR spectra of the three NrGO catalysts. Assumed functional group assignments are labeled. The alkyl C−N frequencies are in the broad structureless feature around 1050 cm^{-1}.

change in the ratio of O−C aromatic bonds along the NrGO series. We also note from the TEM images that the NrGO platelets are not dominated by many holes and hence edge sites. This suggests, but certainly does not prove, that ORR catalysis is dominated by sites on the basal planes rather than at the edge sites.

The overall picture emerging from the combined XPS and HR-TEM is that sp^2 carbon domains are present in all three NrGO catalysts, but at varying extents, and all with similar functional groups (albeit at somewhat different concentrations). This conclusion is strengthened by IR spectroscopic data (Figure 1b) of the three NrGO. This shows nearly identical functional groups, but with somewhat different IR intensities. For example, the peaks assigned to aromatic C=C bonds at ca. 1650 cm^{-1} and alkenes C=C at ca. 1390 cm^{-1} increase significantly in intensity, from NrGO-2, to NrGO-3, to NrGO-4.[18,19] This trend is entirely consistent with the conclusion of increasing sp^2 fraction along the series from NrGO-2 to NrGO-4 obtained from the XPS and TEM. The IR spectroscopic results also show that epoxide and hydroxyl groups along the basal planes coexist in all three samples.[18,19] We argue later that the C sp^2 adjacent to these sites represents the catalytically active surface sites. Given that these three catalysts (will) show very different ORR mechanisms and

selectivity, the XPS, Raman, IR, and HR-TEM characterizations all suggest that the general catalyst structure around active sites is important for determining the ORR mechanism, total activity, and selectivity. This realization is key to all further discussions regarding the NrGO catalysis and also forms the basis for the DFT models discussed below.

Electrical conductivity measurements of NrGO-2, NrGO-3, and NrGO-4 in a thin film (~50 nm) deposited on Si wafer are 0.09, 2.10, and 56.8 S/cm, respectively, and are shown in Figure 1a as a function of the XPS-estimated sp^2 carbon fraction (Table 1). This shows a dramatic increase in electrical conductivity with larger graphene contents. Even more dramatic increases in electrical conductivity with sp^2 carbon fraction have been previously observed in three-monolayer rGO films (Figure 1a).[20] This dramatic increase is most prominent at lower levels of GO reduction (small sp^2 carbon fraction) where conductivity arises from either electron tunneling or hopping between neighboring graphene patches (due to the absence of percolating pathways).[21] We therefore expect that the conductivity of few-monolayer NrGO catalysts will show more extreme variations with the sp^2 carbon fraction as compared to the 50 nm film assembly measured here. The importance of nitrogen doping to the conductivity of more strongly or weakly reduced GO samples has not yet been explored.[22]

Zeta-potentials (ζ-potentials) for the three NrGO electrocatalysts as a function of electrolyte pH are given in Figure S4. ζ-Potentials reflect the local surface charge associated with the double layer around colloidal particles when they are placed in an electrolyte and are strongly correlated with their aqueous dispersibility. Negative surface charging of rGO is usually discussed in terms of the ionization of carboxylic groups at edges.[23] However, as discussed in detail later, negative surface charging on the basal planes of NrGO is also possible through H^+ desorption/OH^- adsorption on dangling C bonds within the graphene domains. Figure S4 indicates that NrGO-2 has a much stronger negative surface charging and that it is strongly pH-dependent. The sign of the ζ-potential and its pH dependence suggests that the dominant surface charging is likely due to OH^- adsorption on the basal planes and COOH ionization at edge sites.

ORR Electrochemistry of NrGO. As discussed in this section, the three different NrGO catalysts show very different behavior in catalyzing the ORR. Widely varying ORR behavior of carbon-based electrocatalysts has generally been observed throughout the literature.[2−7,24] We utilize slow cathodic linear sweep voltammetry (LSV) and chronoamperometry (CA) in an H-cell that isolates the working electrode from the counter electrode to probe the potentials for the ORR onset and selectivity of the NrGO. This setup ensures that the Pt ion diffusion between the electrodes is severely impeded and therefore does not contaminate our ORR results.

Since LSV does not formally separate the kinetic rate from the mass transport rate, we also use LSV of the NrGO drop-cast on a glassy carbon rotating disk electrode (RDE) to isolate the kinetic rate from the mass transport. The differences to simple LSV, however, were minimal. In addition, the observed selectivity seems to be completely unaffected by any mass transport limitations occurring at high currents. Here, it must be stressed that the ensuing mechanistic discussion is focused primarily on the low-current regime (i.e., around ORR onset) where transport limitations are generally negligible. A formal investigation in terms of varying rotation rates is therefore not pursued any further.

Figure S5 shows the simultaneous measurements of total e^- and O_2 moles consumed during a cathodic linear sweep (2.0 mV/s) with a well-mixed oxygen-saturated (~800 torr O_2) electrolytes with pH = 1, 5, 9, and 13 on the three NrGO electrodes. The result implies that NrGO-2 undergoes $2e^-$ ORR [$e^-/O_2 = 2$] (except at very high overpotential), NrGO-4 undergoes $4e^-$ ORR [$e^-/O_2 = 4$], and NrGO-3 undergoes both $2e^-$ and $4e^-$ ORRs with a ratio that depends upon both the overpotential and pH. More accurate e^-/O_2 ratios are obtained using CA. These results are given in Figure 2 for pH

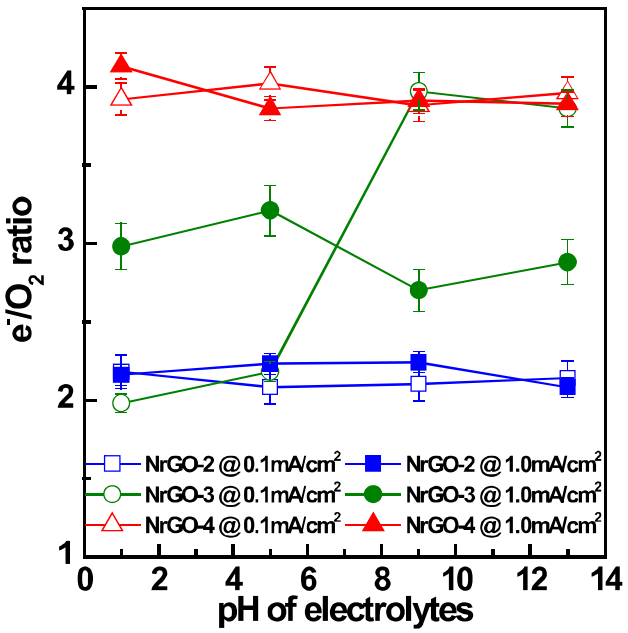

Figure 2. Electron-transfer number (e^-/O_2) for the three NrGO catalysts as a function of pH at both low overpotential and higher overpotential. The overpotentials were selected so that the ORR current density corresponds to 0.1 and 1.0 mA/cm^2. The e^-/O_2 ratio is obtained by the in situ pressure decay measurement of the calibrated volume O_2 headspace during chronoamperometry.

= 1 and 13 and for selected overpotentials that correspond to ORR current densities of 0.1 and 1.0 mA/cm^2, respectively. The three NrGO catalysts clearly have quite different ORR selectivity. NrGO-2 always produces H_2O_2 (HO_2^-) independent of pH and overpotential. NrGO-4 is entirely selective toward producing H_2O independent of pH and overpotential. However, NrGO-3 shows a transition from $2e^-$ ORR in acid to $4e^-$ ORR in base at an ORR current of 0.1 mA/cm^2 and a combination of $2e^-$ and $4e^-$ ORRs with an average number of ~3 electrons consumed per O_2 molecule at an ORR current of 1.0 mA/cm^2.

The pH dependence of ORR observed by LSV for the three NrGO is summarized in Figure 3, where the ORR onsets have quite different behavior with V_{RHE}. The NrGO-2 onset shifts ~59 mV/pH on the RHE scale or equivalently is nearly constant with pH at ~0 V_{SHE} (see Figure S6 for the data plotted versus SHE). In terms of the $2e^-$ ORR thermodynamics, the onsets imply that there is no apparent overpotential at pH = 13, but a ~1 V overpotential at pH = 1. On the other hand, the onset potential for NrGO-4 is invariant

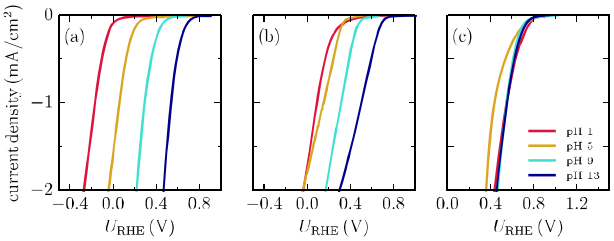

Figure 3. ORR cathodic linear sweep voltammetry (current density in mA/cm^2 vs applied potential U in volts relative to the reversible hydrogen electrode) at the pH values indicated in the figure's legend. Panels (a)−(c) refer to measurements at the NrGO-2, NrGO-3, and NrGO-4 catalysts, respectively.

with pH at ∼0.8 V_{RHE} or equivalently a shift of 59 mV/pH with V_{SHE}. This onset implies a minimum activation overpotential of ∼0.4 V for the 4e$^-$ ORR at all pH (based on the equilibrium potentials given by eqs 1 and 3), i.e., roughly the minimum 4e$^-$ ORR overpotential allowed by the scaling relations.[25,26] Thus, if NrGO-4 is sufficiently stable, it could be an excellent ORR catalyst in acid, as well as base. NrGO-3 ORR is more complicated as our data suggest different processes occurring at varying potentials (as evidenced by the kinks appearing in the corresponding Tafel slopes; Figure S8) and with different behaviors in acid and base. Our interpretation nevertheless suggests that in base the 4e$^-$ occurs with a ∼0 V_{SHE} onset that appears invariant with pH on the SHE scale. In acid, the 2e$^-$ ORR occurs with a ∼0.7 V_{RHE} onset that is invariant with pH on the RHE scale. Figure S7 shows that the ORR of NrGO-3 in acid is identical with and without 1 mM H_2O_2 present. In addition, H_2O_2 with an Ar headspace was stable to a reduction on NrGO-3 over the ORR potential range. This proves that the 4e$^-$ ORR in NrGO-3 does not arise from a series of reduction processes where a 2e$^-$ ORR first forms H_2O_2, which is further reduced on the catalyst to H_2O. In other words, the 2e$^-$ and 4e$^-$ ORRs at NrGO-3 are completely independent processes.

The immediate implications of the pH dependence of ORR onsets suggest a non-CPET mechanism for 2e$^-$ ORR on NrGO-2, a CPET mechanism for 4e$^-$ ORR on NrGO-4, and dominantly a combination of CPET/non-CPET mechanisms in acid/base for the 2e$^-$/4e$^-$ ORR on NrGO-3. The dependence of the ORR kinetic currents on potential as measured by the RDE experiments is given in Figure S8. While this data does not always show a very clear linear dependence of $\log(i)$ on U, we extract and report below approximate Tafel slopes $b = dU/d\log(i)$ for the ongoing ORR process in each case. For NrGO-2, we estimate $b \sim 128$ mV/decade for pH = 1 and ∼60 mV/decade for pH = 13. For NrGO-4, $b \sim 90$ mV/decade at pH = 1 and $b \sim 71$ mV/decade. For NrGO-3, the RDE experiments suggest that two ORR processes (2e$^-$ and 4e$^-$) occur with different onsets and different Tafel slopes, i.e. $b \sim 216$ mV/decade and ∼195 mV/decade at pH = 1 and 13, respectively, near the initial ORR onset and $b \sim 170$ and ∼185 mV/decade at pH = 1 and 13 for the ORR process that seems to occur at ∼0.2 V more reducing potentials than the initial ORR onset. There may be a slight hint in the RDE experiments that NrGO-4 also contains a very small amount of another ORR process (or active site).

The H/D kinetic isotope effect (KIE) helps to identify both the potential-limiting step and the kinetic rate-limiting step in the ORR reaction.[14] The former defines the onset potential for ORR, while the latter defines the ORR current beyond onset, e.g. in the Tafel slope. Figure 4 shows the LSV scans for ORR of the three NrGO at pH(D) = 1 and pH(D) = 13. For NrGO-

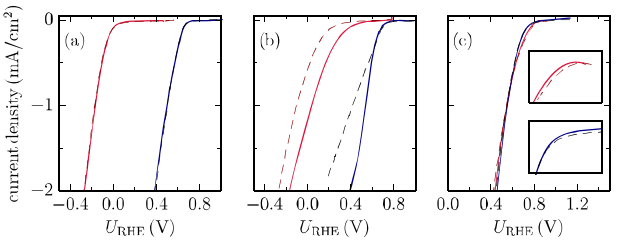

Figure 4. ORR cathodic linear sweep voltammetry (current density in mA/cm^2 vs applied potential U in volts relative to the reversible hydrogen electrode) in protonated (solid lines) and deuterated (dashed lines) solutions. Colored lines are for pH(D) = 1 in crimson (dark red) and pH(D) = 13 in blue (black). Panels (a)−(c) refer to measurements at the NrGO-2, NrGO-3, and NrGO-4 catalysts, respectively. Insets in panel (c) zoom in to magnify the small H/D isotope effect in NrGO-4 for pH(D) = 1 (top) and pH(D) = 13 (bottom).

2, there is no kinetic isotope effect in either the onset potential or apparent Tafel slope at both pH. This suggests that proton transfers are not involved in either the ORR potential-limiting step or the electrochemical kinetics for both pH. At NrGO-4, however, an isotope effect appears in both the ORR onset and apparent Tafel slope at both pH. This suggests proton involvement in both the potential-limiting and kinetic rate-limiting steps at both pH. We quantify the KIE as $i_D/i_H \sim 0.4$ at close-to-zero overpotential conditions, i.e., at ∼0.8 $V_{RHE/RDE}$, while considering also the different standard equilibrium potentials (2.458 V_{RHE} vs 2.524 V_{RDE}) based on the experimental H_2O/D_2O formation free energies[27] (Figure S9). This is nominally an inverse isotope effect ($i_D > i_H$) such as have been previously observed in, e.g., OER[28] and can be rationalized by a ZPE increase at the transition state as compared to the initial reactant state in the rate-limiting step.[14] In NrGO-3, there are very large normal ($i_H > i_D$) isotope effects, both for the ORR onset at pH = 1 and at higher overpotentials at pH = 13. CA experiments measuring e$^-$/O_2 at different overpotentials (Figure S10) suggest that both of these large isotope effects are due to a shift of ∼0.2 V toward higher overpotentials for the 2e$^-$ ORR onset with deuteration. Because of the complexity caused by the two ORR processes, it is not possible to observe isotopic differences in Tafel slopes in NrGO-3.

Based on these experimental results and the understanding that has evolved from the combined experimental and theoretical study of ORR on mrGO,[14] some qualitative conclusions about the mechanisms of ORR are possible. For NrGO-2, the ORR onset is ∼0 V_{SHE} at all pH (Figure S6). This is close to the equilibrium potential for the aqueous electrochemical reduction of O_2 to O_2^- with a likely experimental O_2^-(aq) concentration of 10^{-6} M near the ORR onset. We thus believe that the outer-sphere reduction of O_2 to O_2^-(aq) is the potential-limiting step for the 2e$^-$ ORR at all pH [$O_2 + e^- \rightarrow O_2^-$(aq)], where the conductive support acts as the e$^-$ source. This agrees with the absence of any KIE in the ORR onset. If this step is also kinetically rate-limiting, this predicts a Tafel slope of ∼120 mV/decade neglecting the potential-dependent surface coverage contributions to the kinetics.[29] This agrees qualitatively with the measured value of

b for NrGO-2 at pH = 1. At pH = 13, the ~60 mV/decade Tafel slope suggests that a later chemical step is rate-limiting (i.e., either surface adsorption of O_2^-(aq) or its subsequent protonation to OOH*).[29] Thus, the mechanism at all pH for NrGO-2 should be similar to that determined for non-nitrogen-doped mrGO, i.e., with the NrGO-2 electrode activity functioning as a cocatalyst.[14]

For NrGO-4, the pH dependence of the onset signifies that a CPET step is the potential-limiting one. This interpretation is based on the realization that protons must be directly involved in the ORR electrochemistry[27] and does not preclude, e.g., the existence of a H^+ transfer pre-equilibrium, as discussed in connection to the Pourbaix diagrams in the following section. The KIE also suggests that both the potential-limiting and kinetic rate-limiting steps are CPET steps. From the approximate Tafel slopes determined for this catalyst, it is likely that the rate-limiting step is the first electrochemical step that forms a surface-bound OOH* species, i.e. O_2* + (H^+ + e^-)→OOH*, however, modified strongly by surface coverage effects.[29,30] This assignment would be consistent with the observed inverse isotope effect[14] and weak OOH* binding predicted by theory in the next section.

Finally, for NrGO-3, since both $2e^-$ and $4e^-$ ORRs are present, we suggest that more than one type of site or structure is active in ORR and with different dependences on pH. This type of behavior has, in fact, been observed before for N-doped graphene, but mechanisms were not really discussed or explained.[9] To the extent that the processes can be uncoupled, it appears from the pH dependence of the onsets that the potential-limiting step is a CPET step for $2e^-$ ORR in acid and likely a non-CPET step for $4e^-$ ORR in base. We note, however, that our interpretation at high pH may be skewed by the fact that H_2O is the likely proton source for the ORR at these conditions and this may also introduce a pH dependence when plotted vs V_{RHE}. We further believe it likely that there is a transition between the two (CPET and non-CPET) mechanisms as a function of potential. This scenario, along with the origin of the very strong KIE for the $2e^-$ ORR onset, which underlies the pH dependence of the selectivity at low overpotentials, will be discussed later. In all cases, however, the high Tafel slopes suggest that the rate-limiting steps are the first electron transfers.

DFT Models of the NrGO Electrocatalysts. Guided by the structural characterization of the NrGO samples, we develop qualitative DFT models to rationalize the different ORR mechanisms at these catalysts. On the basis of our HR-TEM, we focus on the basal planes as dominating the ORR activity. According to Figure 1a, the NrGO planes consist of nanometer-sized graphene patches that are interspersed within regions of sp^3 carbon. From the XPS atomic compositions, the latter must be mainly functionalized by oxygen-containing groups that are known to aggregate along the rGO basal planes[31] as O represents the more abundant heteroatom in all three NrGO samples (Table 1). In simplifying the complex oxide structure, we utilize epoxy O groups to represent all disruptions in the aromatic domains. This simplification is justified by our spectroscopic characterization and also by the enhanced stability of on-plane epoxy as compared to hydroxyl groups.[21] We recently used a similar structural motif to explain a wide range of pH-dependent experimental results for the mrGO catalyst,[14] which, as indicated above, produces the same ORR signature as NrGO-2. We argue here that the key mechanistic feature shared by these two catalysts is the underlying rGO framework, which forms isolated graphene patches that render the catalyst semiconducting at operating ORR conditions. We illustrate this effect here by developing theoretical models that follow the XPS-derived trend for the C/O ratios presented in Table 1, while adding (modest) N-doping to the graphene domains to represent NrGO. While these simplified models are certainly far from providing a detailed description of the complex inhomogeneity that characterizes the extended NrGO surface structures, they elucidate critical aspects of the underlying ORR mechanisms that may be relevant to other electrocatalytic reactions as well.

N-Doping of Reduced Graphene Oxide. We first illustrate the general effects of N-doping to rGO by adding N to the graphene patches of our earlier mrGO model illustrated in Figure S11. The density of states (DOS) of mrGO shows localized C defect states that emerge within the semiconducting energy gap (Figure S11). These are associated with the breaking of π-bonds within the sp^2-hybridized graphene domains and form local half-filled states around the Fermi level. This interpretation of "dangling" bonds is confirmed by spin-polarized GGA calculations, which reveal the existence of unpaired electrons. These are generally delocalized over different sp^2 carbon sites, yet predominantly found at the boundary of the graphene–GO region as illustrated by the corresponding spin charge density (Figure S11).

Adding one graphitic N-dopant to this model adds one electron to the carbon π-network (n-type doping) to quench an existing dangling bond (or create a new one when none exists). As a result, the overall spin *S* changes by $\pm 1/2$. This is exemplified by successively adding one, two, and three graphitic N-dopants to the mrGO model (Figures S12–S14). Doping mrGO with pyridinic or pyrrolic N withdraws one electron per N (p-type doping), which again either quenches or creates dangling bonds in a similar manner (Figures S15 and S16). The net spin effect is therefore independent of whether the added N is graphitic, pyridinic, or pyrrolic, i.e., each N-dopant either quenches or adds a dangling bond. We note that this situation is quite different from the 1/2 electron that is added/withdrawn per graphitic/pyridinic N in pure graphene[25,26] and the metallic rGO structures discussed below in connection with the NrGO-4 catalyst.

The existence of dangling bonds plays an important role in defining the equilibrium surface composition in solution. Local graphene patches with a nonzero spin ($S \neq 0$) are naturally active toward adsorption and are therefore most likely covered by H^+/OH^- species in acid/base. On the other hand, graphene patches with no spin polarization ($S = 0$) may or may not bind H^+/OH^-. In either case, the new bond formed upon adsorption withdraws an electron from the substrate's π-network and will, in turn, either quench an existing dangling bond or create a new one. These general remarks are established by investigating a variety of more than 10 NrGO structure models as further discussed in the Supporting Information. The conclusions are therefore not specific to a particular structural configuration and thus form the basis for H^+/OH^- surface coverages used in discussing the NrGO ORR. It is this fact that justifies the use of simple representative models to discuss the mechanisms on the generally complicated NrGO catalysts.

NrGO-2 Catalyst and ORR. Figure 5A–D shows a set of simple model structures to represent the catalytic NrGO-2 surface. While incorporating different concentrations of O and

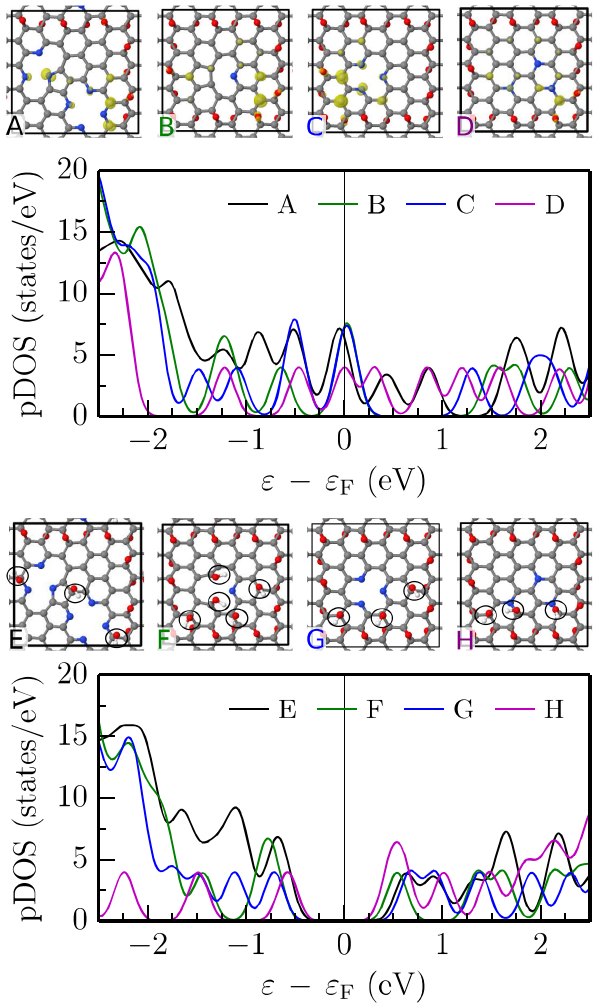

Figure 5. Theoretical models for the catalytic NrGO-2 surface. Panels (A–H) show the (A–D) clean and (E–H) corresponding saturated structures with overlaid isosurface of the spin electron density (cutoff 0.05 Å^{-3}) in yellow. The box shows the repeated unit cell in the DFT calculations, while gray, red, yellow, and white spheres represent C, O, N, and H atoms, respectively. Circles identify the adsorbed OH^-(aq) in panels (E–H) due to alkaline conditions, pH = 13. Plotted below each set of structures is the corresponding projected density of states (pDOS) in eV^{-1} vs energy relative to the Fermi level.

N heteroatoms, the common feature underlying all of these models is a separating GO region, which insulates the neighboring graphene domains from one another (note the applied periodic boundary conditions). This picture is consistent with the lowest experimental fraction of sp^2 carbon (~0.5) in NrGO-2 and the corresponding prediction of a low conductivity framework (Figure 1a). The model of Figure 5A is specifically constructed by considering the average atomic composition measured in XPS (Table 1) and shall be discussed first. We include here only pyridinic/pyrrolic N-species within the graphitic domains with a fraction of C/N ~ 7.1 as these are suggested as the dominant dopant types in this sample (Table 1).

Calculation of the DOS for this NrGO-2 model structure is outlined in black in the top DOS panel of Figure 5. This DOS predicts one unpaired electron (S = 1/2) that is delocalized over different C and N atoms as illustrated by the overlaid spin charge density in Figure 5A. These sites are most active toward adsorption and are likely covered by H^+ or OH^- species in solution. Competitive oxygen adsorption is not considered relevant for these electrocatalysts as we consistently predict H*/OH* to outcompete O* species in occupying the available surface sites under reducing ORR conditions (Figure S61). The adsorption of sequential OH^- from alkaline solution quenches and then creates new dangling bonds at the surface with ±1/2 changes in spin (Figures S17–S20). Whether this actually occurs, however, depends on the thermodynamics of adsorption from the aqueous solution as given by the surface Pourbaix diagrams. Figure 6 shows the surface Pourbaix

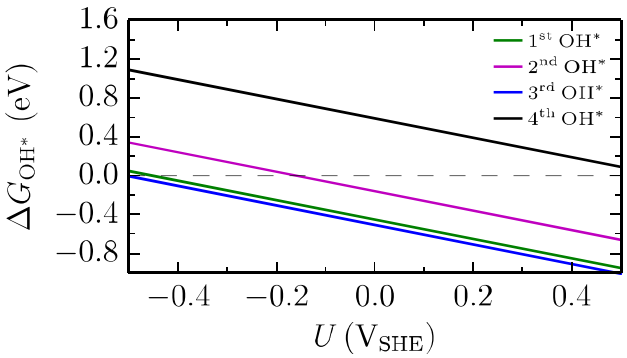

Figure 6. Pourbaix diagram (free energy of adsorption vs potential U in volts relative to the standard hydrogen electrode) depicting the relative stability for the sequential adsorption of OH^-(aq) species at the NrGO-2 model structure depicted in Figure 5A in alkaline solution, pH = 13. In each case, the most favorable adsorption sites are considered and the estimated OH* solvation correction of −0.4 eV is included.

diagram for the sequential adsorption of a first, second, third, and fourth OH^- species for this particular model NrGO-2 structure at pH = 13, with adsorption always occurring on the most favorable site. This suggests that the adsorption of the first three OH^- species is exoergic ($\Delta G_{OH^*} < 0$), beyond which point the surface becomes saturated so that further adsorption is no longer thermodynamically favorable ($\Delta G_{OH^*} > 0$). The resulting structure with three OH* is shown in Figure 5E and found to be fully semiconducting with a GGA–DFT band gap of ~1 eV (lower DOS plot of Figure 5).

Similar conclusions are reached for adsorbing H^+(aq) species in acid. The corresponding analysis shows continued H^+ adsorption until the surface is saturated with the concomitant opening of a semiconducting band gap (Figures S21 and S22). One difference to be noted here is that H^+ can adsorb on both C and pyridinic/pyrrolic N sites so that a larger number of adsorption events are possible. The band-gap opening also persists regardless of the concentration or type of the N-dopants within the graphitic patch, as exemplified by the corresponding analyses for the structural models of Figure 5B–D (Figures S23–S34). This result remains unchanged also when simulating larger NrGO-2 structural models (Figure S62). The overall picture that emerges therefore is that under operating ORR conditions in acid or base, the NrGO-2 catalyst adsorbs H^+ or OH^- until there is no remaining electron density at the Fermi level, i.e., conceptually similar to the mrGO model described previously.[14]

This picture agrees with the low electrical conductivity measured for the NrGO-2 sample (Figure 1a) and implies slow

e^- transfer from the conducting support to the semiconducting catalytically active sites. Because of this, we exclude the possibility of a CPET mechanism to describe the ORR, as recently argued for the $2e^-$ ORR at mrGO/P50.[14] Predicting the limiting ORR potential on the basis of a thermodynamic descriptor such as the adsorption free energy of the OOH* intermediate is not applicable in this situation.[32] Based on the weak OOH* binding at the OH-saturated NrGO-2 models, a thermodynamic analysis of CPET would result in large $\eta >$ ~0.6 V overpotentials that are incompatible with the experimental $\eta <$ 0.1 V in base (cf. the activity volcano plot in Figure S35). A non-CPET mechanism is therefore entirely consistent with the experiments, which suggest that the potential-limiting step in the NrGO-2 ORR is an initial outer-sphere electron transfer to O_2 in solution from the conducting support. In analogy to mrGO/P50,[14] this initial electron transfer is followed by diffusion and subsequent surface adsorption of either O_2^-(aq) or HO_2(aq) depending upon pH. As the latter is a chemical step, weak binding at the saturated NrGO-2 surface only enters this model as a kinetic barrier and does not affect the limiting ORR potential.

The emerging picture suggests that the catalytically active sites at NrGO-2 are most likely defined as those that are most reactive toward adsorbing O_2^- (in base) or HO_2 (in acid) from solution. Investigating the OOH* binding strength for the H-saturated surfaces in acid identifies these sites as sp^2 carbons that are located next to epoxides, i.e., at the boundary of the graphene and GO regions (Figure S36). Based on our detailed thermodynamic analysis of mrGO, we believe that the strongest OOH* binding is correlated to the strongest $[O_2^-]$* binding and can thus similarly predict the most active ORR sites also in base.[14] A corresponding analysis at the OH-saturated surfaces generally shows that the active sites are found at different locations as compared to the H-saturated surfaces, yet consistently lying at the boundaries of the sp^2–sp^3 carbon regions (Figure S37). This is exactly the same catalytically active site that was found responsible for $2e^-$ ORR at mrGO.[15] As also suggested by our recent spectroscopic characterization,[33] we therefore conclude that it is not the nitrogen- but rather the oxygen-containing functional groups such as epoxies that dominate ORR activity toward H_2O_2 formation at (mildly reduced) NrGO.

NrGO-4 Catalyst and ORR. At high sp^2 carbon fractions in rGO, we anticipate a C–O framework with weakly conducting links between the graphene patches as discussed in ref 20. This is also evident in the TEM of NrGO-4 (Figure S3). Figure 7A–D shows the model NrGO-4 structures that incorporate this feature so that the N-doped graphene patches are interconnected via sp^2 carbon channels. Among these, the model of Figure 7A is specifically constructed based on the average atomic composition measured from XPS and includes a low concentration of the dominant graphitic N-species (C/N ~ 29.0) according to Table 1. The DOS for this particular structure is outlined in black in the top DOS panel of Figure 7 and shows considerable electron density at the Fermi level. The extent of OH^-/H^+ adsorption from solution is again determined by the Pourbaix diagrams (Figures S40 and S43). These imply that at the onset of ORR at pH = 13, i.e., at V_{RHE} ~ 0.8 (V_{SHE} ~ 0.0), a single OH^- is adsorbed as shown in Figure 7E. At the corresponding ORR onset at pH = 1, i.e., at V_{RHE} ~ 0.8 (V_{SHE} ~ 0.7), no H^+ is adsorbed. Importantly, our analysis shows that this structure retains its metallic character in solution (lower DOS plot of Figure 7) and even when

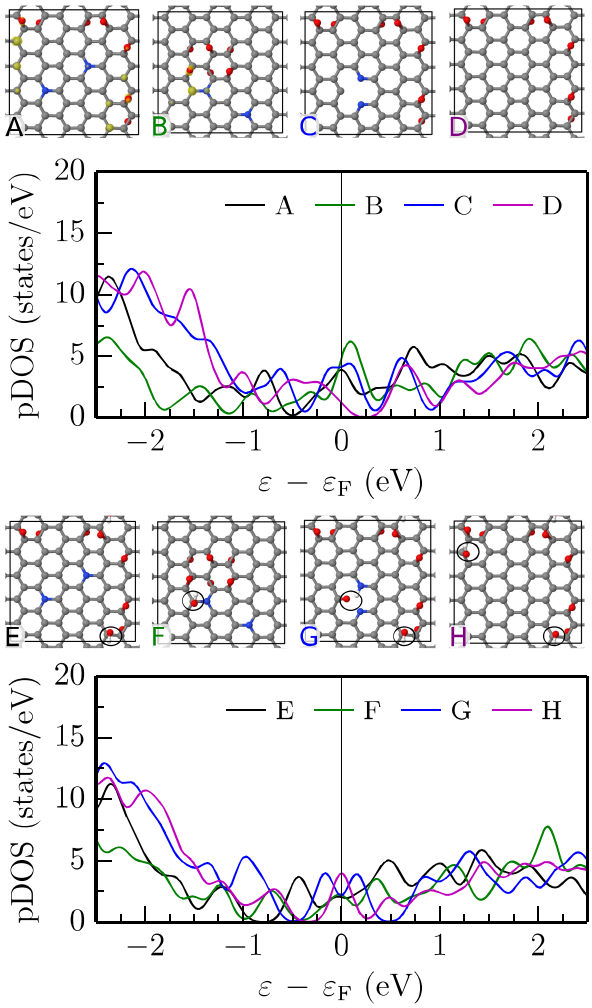

Figure 7. Theoretical models for the catalytic NrGO-4 surface. Panels (A–H) show the (A–D) clean and (E–H) corresponding saturated structures with the overlaid isosurface of the spin electron density (cutoff 0.05 $Å^{-3}$) in yellow. The box shows the repeated unit cell in the DFT calculations, while gray, red, yellow, and white spheres represent C, O, N, and H atoms, respectively. Circles identify the adsorbed OH^-(aq) in panels (E–H) due to alkaline conditions, pH = 13. Plotted below each set of structures is the corresponding projected density of states (pDOS) in eV^{-1} vs energy relative to the Fermi level.

considering further OH^-/H^+ adsorption events that are endothermic (Figures S39 and S42). The same conclusion is drawn from the corresponding analyses on additional structural models (Figures S45–S59) that, e.g., include pyridinic N (Figure 5C) or no N-doping at all (Figure 5D), also when considering larger unit cells (Figure S63). Therefore, the existence of conducting links between the graphene patches ensures that the electronic structure remains metallic regardless of the structural details.

The metallic character of the NrGO-4 catalyst allows ORR to occur as a CPET process, in agreement with the experimental results discussed previously. The catalytic activity for the $4e^-$ CPET ORR is then determined by the binding energies of OH*, O*, and OOH* reaction intermediates, all of which are usually correlated by linear scaling relations that allow expressing the catalytic activity via a single thermodynamic descriptor.[25,26] These scaling relations imply a minimum

overpotential of ~0.37 V for the CPET 4e⁻ ORR. Given the 1.23 V_{RHE} equilibrium potential (eqs 1 and 3), this translates into a ~0.86 V limiting potential (U_{lim}) that defines the top of activity volcano plots for the full 4e⁻ ORR (Figure 8 below).

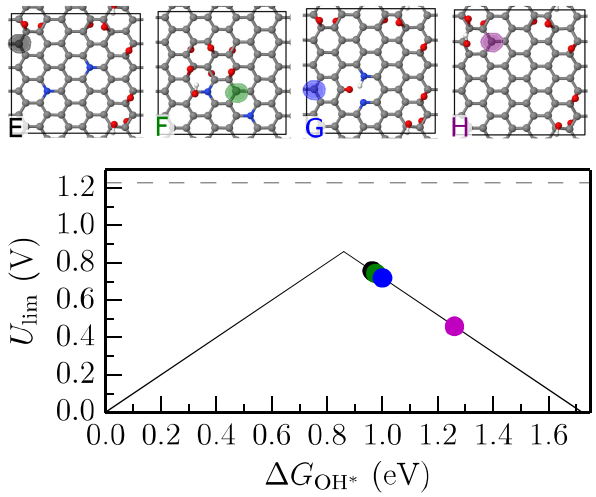

Figure 8. Volcano plot for the 4e⁻ ORR where the limiting potential is plotted as a function of the free energy of the adsorbed OH* intermediate (incl. the estimated solvation correction of −0.4 eV). Colored circles describe the different adsorption sites that are marked correspondingly on the NrGO-4 model structures in panels (E−H). The equilibrium ORR potential is depicted by the dashed line at 1.23 V_{RHE}, while the top of the volcano at 0.86 V_{RHE} represents the ideal catalyst with a minimum overpotential of 0.37 V due to OOH*/O*/OH* scaling relations.

Figure S41 compares the explicitly calculated OH*, O*, and OOH* binding energies to the values predicted from scaling at the most active site on the NrGO-4E model catalyst. This shows that the general scaling relations derived for ORR on metal and alloy systems seem to also be valid for these NrGO catalysts as well. The activity volcano plot (Figure 8) based on the scaling relations represents the theoretical U_{lim} predicted as a function of the OH* adsorption free energy (ΔG_{OH^*}) calculated at the most active surface site for each of the OH-saturated model structures presented above (Figure 8E−H). The most active sites are found to lie within ~0.1−0.2 V of the top of the volcano (U_{lim} ~ 0.86 V) so that their activity is similar to those of many known precious-metal catalysts.[11] Since U_{lim} is essentially the onset potential for ORR, U_{lim} calculated for the 4e⁻ ORR is in excellent agreement with that observed experimentally for NrGO-4 (Figure 3).

Strikingly, Figure 8E−H shows that it is again the sp^2 carbons located next to epoxides that are responsible for catalyzing this 4e⁻ ORR at NrGO-4. Despite the predominant role of the oxygen functional groups, the presence of N-dopants can affect the ORR activity (and possibly also selectivity) by modifying the chemical environment around the catalytically active site. Limited ORR activity, for example, is predicted for the rGO model of Figure 8H, which has an identical C−O framework to that of Figure 8E, but does not include N-doping. This effect most likely arises from an increased electron density due to substitutional (n-type) doping in NrGO-4A (Figure S60). Additional NrGO-4 configurations tested (that also resemble the compositions of Table 1) also showed a varying U_{lim} and thus further confirm the importance of the general chemical environment around the active site (Figures S54−S59). These observations are in line with an experimental study suggesting that the chemical nature and amount of N-dopants control the activity toward the 4e⁻ ORR in NrGO.[34] Since the NrGO-4 catalyst has a mixture of structures fulfilling the overall composition, those regions with the structure outlined in our models of NrGO-4 or other ones with an equivalent U_{lim} ~ 0.8 V_{RHE} likely dominate the observed ORR.

NrGO-3 Catalyst and ORR. Because NrGO-3 has both 2e⁻ and 4e⁻ catalytical activities, with apparent CPET and either CPET or non-CPET mechanisms, respectively, we believe that NrGO-3 must represent the heterogeneity of the catalyst so that we will not try to construct a single structural model to simultaneously describe both ORR processes. We believe that some regions of the catalyst flake must be metallic like those of NrGO-4 to account for CPET 2e⁻ and CPET 4e⁻ ORRs. However, other regions of the catalyst may be semiconducting like NrGO-2 to account for a non-CPET 4e⁻ ORR. Note that nothing in the NrGO-2 and NrGO-4 models describes the 2e⁻ vs 4e⁻ ORR selectivity so that all of these models would be compatible with either 2e⁻ or 4e⁻ ORR. At low pH, the 2e⁻ ORR process has the highest onset potential, while at high pH, the 4e⁻ ORR has the highest onset potential. However, at more reducing potentials, both seem to occur with roughly the same activity. At high pH, it is possible that the outer-sphere O_2 reduction is the potential-limiting step just as in NrGO-2 and that this ultimately produces H_2O in a 4e⁻ reduction with a ~0.4 V overpotential. This is consistent with the absence of a H/D isotope effect in the onset potential for the 4e⁻ ORR process in NrGO-3. Transition to a CPET mechanism at more reducing potentials would also be consistent with metallic catalyst regions dominating the ORR activity as OH* species are removed from the surface in accordance with the demonstrated Pourbaix diagrams. At low pH, there is a substantial activation overpotential for the pure electron-transfer process describing $O_2 + e^- \rightarrow O_2^-$ (aq) so that it may no longer correspond to the route of lowest overpotential. Instead, a CPET process has the lowest overpotential, and the very large isotope effect in the onset potential at low pH and at more reducing potentials at high pH imply coupled proton−electron transfers as the potential-limiting step for the 2e⁻ ORR process in NrGO-3.

■ CONCLUSIONS

We have presented three different preparations of NrGO catalysts supported on conducting P50 carbon paper, NrGO-2, NrGO-3, and NrGO-4, all with very different ORR properties. We have studied the pH-dependent ORR selectivity, onset potentials for ORR, Tafel slopes, and H/D kinetic isotope effects. These results suggest that the mechanism for NrGO-2 is a non-CPET 2e⁻ ORR, for NrGO-4 a 4e⁻ CPET ORR and for NrGO-3 both a 2e⁻ CPET and 4e⁻ either CPET or non-CPET ORR contribute, with the lowest overpotential process depending upon pH. Thus, these results illustrate the strong variety in ORR selectivity and mechanisms possible with carbon-based catalysts.

We structurally characterized the catalysts by combining XPS, Raman, and IR spectroscopies with HR-TEM. Despite the different synthesis routes, we find that all three NrGO samples are similar in terms of the identity of (oxygen and nitrogen) functional groups, albeit with some differences in concentrations. The most significant difference lies in the

fraction of sp^2 carbon along the series (in order) NrGO-2 to NrGO-3 to NrGO-4, and this is reflected in the measured thin-film electrical conductivity of the series. This finding is confirmed by HR-TEM, which clearly shows a similarly increasing extent of the sp^2 carbon domains that are embedded within the surrounding sp^3 domains on the basal planes.

Structural models for NrGO-2 and NrGO-4 were constructed based on the spectroscopy and HR-TEM results, and DFT was used to explore which features of the structure determine the ORR mechanism. A critical aspect is the availability of electron density at the Fermi energy of the catalyst, or equivalently electrical conductivity of the NrGO, that largely determines whether a CPET process will dominate. If the catalyst is semiconducting, then the only initial ORR process possible is based on an outer-sphere reduction of O_2(aq) to O_2^-(aq), with the source of the electron being the conducting support. Following this initial electron transfer, O_2^- or HO_2 (depending upon the pH) will adsorb on the semiconducting NrGO, followed by other further decoupled proton−electron transfers to complete the ORR process. On the other hand, if there is sufficient electron density or electrical conductivity, then CPET will likely dominate because the barriers for ORR are generally lower for coupled proton−electron steps than uncoupled steps.[32] We believe that the key to conductivity is the underlying structure of the rGO so that the specifics of (modest) N-doping are not the determining factors in this aspect. It is important to emphasize that all qualitative conclusions made with respect to the ORR mechanisms are also not specific to a particular structural configuration of, e.g., the type and/or distribution of N-dopants, as meticulously tested by investigating a large number of different DFT structural models.

Importantly, regardless of the reaction mechanism or electrolyte pH, we identify sp^2 carbon sites that are located next to oxide regions as dominating the ORR activity. This assignment underlines the importance of oxygen rather than nitrogen functional groups and agrees with our recent experimental characterization using ^{13}carbon nuclear magnetic resonance coupled with magic angle spinning and cross polarization.[33] It needs to be emphasized that the identified ORR active site at NrGO is quite different from the N-adjacent carbons that have been assigned as most active in studies of N-doped graphene catalysts (cf. for example, refs 35−39). Our analysis shows that the most reactive sites at the clean NrGO catalysts are correlated to the local increase in spin density and are therefore predominantly found either at the boundaries of the sp^2−sp^3 carbon regions or adjacent to the N-dopants. However, surface Pourbaix diagrams suggest that these sites are typically covered by H^+/OH^- species at operating ORR conditions, and ultimately, it is the (more abundant) sp^2 sites next to the sp^3 carbon regions that dominate the catalytic activity. Overall, however, the ORR activity (and possibly also selectivity) depends on the general chemical environment around the active site and hence also the presence of N-dopants as has also been observed experimentally.[34]

The origin of ORR selectivity is still poorly understood, both in this work and in our view in all other ORR studies to date. This is true not only for carbon-based catalysts, but for metal/alloy catalysts as well. Thermodynamics always favors the $4e^-$ ORR over the $2e^-$ ORR. However, since $2e^-$ ORR is also sometimes observed, selectivity must originate in the kinetics of ORR, either in the quantitative aspects of the electrochemical barriers or in different ORR mechanisms. Since the theoretical prediction of electrochemical barriers with chemical accuracy is still lacking, the understanding of the origin of ORR selectivity remains a major challenge to the theoretical understanding of ORR.

AUTHOR INFORMATION

Corresponding Authors

*E-mail: acluntz@stanford.edu (A.C.L.).
*E-mail: bmcclosk@berkeley.edu (B.D.M.).

ORCID

Hyo Won Kim: 0000-0001-7385-796X
Vanessa J. Bukas: 0000-0002-0105-863X
Kyle M. Diederichsen: 0000-0002-6787-7996
Jinkyu Lim: 0000-0002-1875-659X
Young Hoon Cho: 0000-0002-8863-1979
Wooyul Kim: 0000-0002-8130-5441
Tae Hee Han: 0000-0001-5950-7103
Johannes Voss: 0000-0001-7740-8811
Alan C. Luntz: 0000-0002-1003-1914
Bryan D. McCloskey: 0000-0001-6599-2336

Present Address

[¶]Catalysis Theory Center, Department of Physics, Technical University of Denmark, DK-2800 Lyngby, Denmark (V.J.B.).

Author Contributions

[⋈]H.W.K. and V.J.B. contributed equally to this work.

Author Contributions

H.W.K. contributed to experimental planning, experimental measurements, data analysis, and manuscript preparation. V.J.B. contributed to developing the theoretical models, data analysis, and manuscript preparation. H.P. synthesized the NrGO-2 material. S.J.P. helped to measure the FT-IR. K.D.D. performed ICP-OES. J.L. helped to perform the RDE experiments. Y.H.C. and H.W.Y. helped to prepare the NrGO materials. J.V. contributed to the computer simulations. W.K. and T.H.H. provided experimental guidance for the NrGO-2 synthesis and the FT-IR characterization, respectively. A.C.L. and B.D.M. contributed to the data analysis and manuscript preparation. All authors reviewed and commented on the manuscript prior to publication.

Notes

The authors declare no competing financial interest.

ACKNOWLEDGMENTS

B.D.M. and H.W.K. gratefully acknowledge support from the National Science Foundation under grant number CBET-1604927. H.W.K. also acknowledges support from the Basic

Science Research Program through the National Research Foundation of Korea funded by the Ministry of Education (2016R1A6A3A03012382). This work was supported, in part, by the U.S. Department of Energy, Chemical Sciences, Geosciences, and Biosciences (CSGB) Division of the Office of Basic Energy Sciences, via Grant DE-AC02-76SF00515 to the SUNCAT Center for Interface Science and Catalysis. This research used resources of the National Energy Research Scientific Computing Center, a DOE Office of Science User Facility supported by the Office of Science of the U.S. Department of Energy under Contract No. DE-AC02-05CH11231. T.H.H. and H.P. gratefully acknowledge support from the National Research Foundation of Korea (NRF) grant funded by the Korea Government (MSIT) (2016R1A6A1A03013422). Work at the Molecular Foundry was supported by the Office of Science, Office of Basic Energy Sciences, of the U.S. Department of Energy under Contract No. DE-AC02-05CH11231.

■ REFERENCES

(1) Bard, A. J.; Parsons, R.; Jordan, J. *Standard Potentials in Aqueous Solution*; Marcel Dekker, Inc.: NY, 1985.

(2) Dai, L.; Xue, Y.; Qu, L.; Choi, H.-J.; Baek, J.-B. Metal-Free Catalysts for Oxygen Reduction Reaction. Chemical Reviews. *Chem. Rev.* **2015**, *115*, 4823−4892.

(3) Geng, D.; Ding, N.; Hor, T. A.; Liu, Z.; Sun, X.; Zong, Y. Potential of Metal-Free "Graphene Alloy" As Electrocatalysts for Oxygen Reduction Reaction. *J. Mater. Chem. A* **2015**, *3*, 1795−1810.

(4) Inagaki, M.; Toyoda, M.; Soneda, Y.; Morishita, T. Nitrogen-Doped Carbon Materials. *Carbon* **2018**, *132*, 104−140.

(5) Gewirth, A. A.; Varnell, J. A.; DiAscro, A. M. Nonprecious Metal Catalysts for Oxygen Reduction in Heterogeneous Aqueous Systems. *Chem. Rev.* **2018**, *118*, 2313−2339.

(6) Kong, X.-K.; Chen, C.-L.; Chen, Q.-W. Doped Graphene for Metal-Free Catalysis. *Chem. Soc. Rev.* **2014**, *43*, 2841−2857.

(7) Wang, H.; Maiyalagan, T.; Wang, X. Review on Recent Progress in Nitrogen-Doped Graphene: Synthesis, Characterization, and Its Potential Applications. *ACS Catal.* **2012**, *2*, 781−794.

(8) Yang, S.; Verdaguer-Casadevall, A.; Arnarson, L.; Silvioli, L.; Čolić, V.; Frydendal, R.; Rossmeisl, J.; Chorkendorff, I.; Stephens, I. E. Toward The Decentralized Electrochemical Production of H_2O_2: A Focus on The Catalysis. *ACS Catal.* **2018**, *8*, 4064−4081.

(9) Bai, J.; Zhu, Q.; Lv, Z.; Dong, H.; Yu, J.; Dong, L. Nitrogen-Doped Graphene As Catalysts and Catalyst Supports for Oxygen Reduction in Both Acidic and Alkaline Solutions. *Int. J. Hydrogen Energy* **2013**, *38*, 1413−1418.

(10) Nørskov, J. K.; Rossmeisl, J.; Logadottir, A.; Lindqvist, L.; Kitchin, J. R.; Bligaard, T.; Jonsson, H. Origin of The Overpotential for Oxygen Reduction at A Fuel-Cell Cathode. *J. Phys. Chem. B* **2004**, *108*, 17886−17892.

(11) Kulkarni, A.; Siahrostami, S.; Patel, A.; Nørskov, J. K. Understanding Catalytic Activity Trends in The Oxygen Reduction Reaction. *Chem. Rev.* **2018**, *118*, 2302−2312.

(12) Viswanathan, V.; Hansen, H. A.; Rossmeisl, J.; Nørskov, J. K. Unifying The $2e^-$ and $4e^-$ Reduction of Oxygen on Metal Surfaces. *J. Phys. Chem. Lett.* **2012**, *3*, 2948−2951.

(13) Chan, K.; Nørskov, J. K. Electrochemical Barriers Made Simple. *J. Phys. Chem. Lett.* **2015**, *6*, 2663−2668.

(14) Bukas, V. J.; Kim, H. W.; Sengpiel, R.; Knudsen, K. B.; Voss, J.; McCloskey, B. D.; Luntz, A. C. Combining Experiment and Theory to Unravel The Mechanism of Two-Electron Oxygen Reduction at A Selective and Active Co-catalyst. *ACS Catal.* **2018**, *8*, 11940−11951.

(15) Kim, H. W.; Ross, M. B.; Kornienko, N.; Zhang, L.; Guo, J.; Yang, P.; McCloskey, B. D. Efficient Hydrogen Peroxide Generation Using Reduced Graphene Oxide-Based Oxygen Reduction Electrocatalysts. *Nat. Catal.* **2018**, *1*, 282−290.

(16) Ferrari, A. C. Raman Spectroscopy of Graphene and Graphite: Disorder, Electron−Phonon Coupling, Doping and Nonadiabatic Effects. *Solid State Commun.* **2007**, *143*, 47−57.

(17) Mkhoyan, K. A.; Contryman, A. W.; Silcox, J.; Stewart, D. A.; Eda, G.; Mattevi, C.; Miller, S.; Chhowalla, M. Atomic and Electronic Structure of Graphene-Oxide. *Nano Lett.* **2009**, *9*, 1058−1063.

(18) Acik, M.; Lee, G.; Mattevi, C.; Chhowalla, M.; Cho, K.; Chabal, Y. J. Unusual Infrared-Absorption Mechanism in Thermally Reduced Graphene Oxide. *Nat. Mater.* **2010**, *9*, 840−845.

(19) Acik, M.; Lee, G.; Mattevi, C.; Pirkle, A.; Wallace, R. M.; Chhowalla, M.; Cho, K.; Chabal, Y. The Role of Oxygen During Thermal Reduction of Graphene Oxide Studied by Infrared Absorption Spectroscopy. *J. Phys. Chem. C* **2011**, *115*, 19761−19781.

(20) Mattevi, C.; Eda, G.; Agnoli, S.; Miller, S.; Mkhoyan, K. A.; Celik, O.; Mastrogiovanni, D.; Granozzi, G.; Garfunkel, E.; Chhowalla, M. Evolution of Electrical, Chemical, and Structural Properties of Transparent and Conducting Chemically Derived Graphene Thin Films. *Adv. Funct. Mater.* **2009**, *19*, 2577−2583.

(21) Pei, S.; Cheng, H.-M. The Reduction of Graphene Oxide. *Carbon* **2012**, *50*, 3210−3228.

(22) Li, C.; Hu, Y.; Yu, M.; Wang, Z.; Zhao, W.; Liu, P.; Tong, Y.; Lu, X. Nitrogen Doped Graphene Paper As a Highly Conductive, and Light-Weight Substrate for Flexible Supercapacitors. *RSC Adv.* **2014**, *4*, 51878−51883.

(23) Konkena, B.; Vasudevan, S. Understanding Aqueous Dispersibility of Graphene Oxide and Reduced Graphene Oxide through pKa Measurements. *J. Phys. Chem. Lett.* **2012**, *3*, 867−872.

(24) Čolić, V.; Yang, S.; Révay, Z.; Stephens, I. E.; Chorkendorff, I. Carbon Catalysts for Electrochemical Hydrogen Peroxide Production in Acidic Media. *Electrochim. Acta* **2018**, *272*, 192−202.

(25) Abild-Pedersen, F.; Greeley, J.; Studt, F.; Rossmeisl, J.; Munter, T.; Moses, P. G.; Skulason, E.; Bligaard, T.; Nørskov, J. K. Scaling Properties of Adsorption Energies for Hydrogen-Containing Molecules on Transition-Metal Surfaces. *Phys. Rev. Lett.* **2007**, *99*, No. 016105.

(26) Rossmeisl, J.; Logadottir, A.; Nørskov, J. K. Electrolysis of Water on (Oxidized) Metal Surfaces. *Chem. Phys.* **2005**, *319*, 178−184.

(27) Malko, D.; Kucernak, A. Kinetic Isotope Effect in The Oxygen Reduction Reaction (ORR) over Fe-N/C Catalysts under Acidic and Alkaline Conditions. *Electrochem. Commun.* **2017**, *83*, 67−71.

(28) Tse, E. C. M.; Hoang, T. T. H.; Varnell, J. A.; Gewirth, A. A. Observation of An Inverse Kinetic Isotope Effect in Oxygen Reduction Electrochemsitry. *ACS Catal.* **2016**, *6*, 5706−5714.

(29) Fletcher, S. Tafel Slopes from First Principles. *J. Solid State Electrochem.* **2009**, *13*, 537−549.

(30) Holewinski, A.; Linic, S. Elementary Mechanisms in Electrocatalysis: Revisiting The ORR Tafel Slope. *J. Electrochem. Soc.* **2012**, *159*, H864−H870.

(31) Zhou, S.; Bongiorno, A. Epigraphene: Epitaxial Graphene on Silicon Carbide. *Sci. Rep.* **2013**, *3*, No. 2484.

(32) Koper, M. T. Theory of Multiple Proton−Electron Transfer Reactions and Its Implications for Electrocatalysis. *Chem. Sci.* **2013**, *4*, 2710−2723.

(33) Kim, H. W.; Park, H.; Roh, J. S.; Shin, J. E.; Lee, T. H.; Zhang, L.; Cho, Y. H.; Yoon, H. W.; Bukas, V. J.; Guo, J.; Park, H. B.; Han, T. H.; McCloskey, B. D. Carbon Defect Characterization of Nitrogen-Doped Reduced Graphene Oxide Electrcatalysts for The Two Electron Oxygen Reduction Reaction. *Chem. Mater.* **2019**, *31*, 3967−3973.

(34) Bag, S.; Raj, C. R. On The Electrocatalytic Activity of Nitrogen-Doped Reduced Graphene Oxide: Does The Nature of Nitrogen Really Control The Activity Towards Oxygen Reduction? *J. Chem. Sci.* **2016**, *128*, 339−347.

(35) To, J. W.; Ng, J. W. D.; Siahrostami, S.; Koh, A. L.; Lee, Y.; Chen, Z.; Fong, K. D.; Chen, S.; He, J.; Bae, W.-G.; et al. High-Performance Oxygen Reduction and Evolution Carbon Catalysis: From Mechanistic Studies to Device Integration. *Nano Res.* **2017**, *10*, 1163−1177.

(36) Reda, M.; Hansen, H. A.; Vegge, T. DFT Study of Stabilization Effects on N-Doped Graphene for ORR. Catalysis. *Catal. Today* **2018**, *312*, 118−125.
(37) Zhang, L.; Xia, Z. Mechanisms of Oxygen Reduction Reaction on Nitrogen-Doped Graphene for Fuel Cells. *J. Phys. Chem. C* **2011**, *115*, 11170−11176.
(38) Li, M.; Zhang, L.; Xu, Q.; Niu, J.; Xia, Z. N-dope Graphene As Catalysts for Oxygen Reduction and Oxygen Evolution Reactions: Theoretical Considerations. *J. Catal.* **2014**, *314*, 66−72.
(39) Studt, F. The Oxygen Reduction Reaction on Nitrogen-Doped Graphene. *Catal. Lett.* **2013**, *143*, 58−60.